AGU PUBLICATIONS

JGR

Journal of Geophysical Research: Atmospheres

RESEARCH ARTICLE
10.1002/2017JD026728

Key Points:
- Last millennium climate model simulations produce robust Northern Hemisphere surface winter warming response after large tropical volcanic eruptions
- Last millennium climate model simulations show significant reduction of the summer monsoon after large tropical volcanic eruptions
- The simulated responses depend strongly on the model and choice of the forcing data set

Supporting Information:
- Supporting Information S1

Correspondence to:
B. Zambri,
bzambri@envsci.rutgers.edu

Citation:
Zambri B., A. N. LeGrande, A. Robock, and J. Slawinska (2017), Northern Hemisphere winter warming and summer monsoon reduction after volcanic eruptions over the last millennium, *J. Geophys. Res. Atmos.*, *122*, 7971–7989, doi:10.1002/2017JD026728.

Received 27 FEB 2017
Accepted 25 JUL 2017
Accepted article online 28 JUL 2017
Published online 10 AUG 2017

Northern Hemisphere winter warming and summer monsoon reduction after volcanic eruptions over the last millennium

Brian Zambri[1], Allegra N. LeGrande[2], Alan Robock[1], and Joanna Slawinska[1]

[1]Department of Environmental Sciences, Rutgers University, New Brunswick, New Jersey, USA, [2]NASA Goddard Institute for Space Studies, New York, New York, USA

Abstract Observations show that all recent large tropical volcanic eruptions (1850 to Present) were followed by surface winter warming in the first Northern Hemisphere (NH) winter after the eruption. Recent studies show that climate models produce a surface winter warming response in the first winter after the largest eruptions but require a large ensemble of simulations to see significant changes. It is also generally required that the eruption be very large, and only two such eruptions occurred in the historical period: Krakatau in 1883 and Pinatubo in 1991. Here we examine surface winter warming patterns after the 10 largest volcanic eruptions between 850 and 1850 in the Paleoclimate Modeling Intercomparison Project 3 last millennium simulations and in the Community Earth System Model Last Millennium Ensemble. These eruptions were all larger than those since 1850. Though the results depend on both the individual models and the forcing data set used, we have found that models produce a surface winter warming signal in the first winter after large volcanic eruptions, with higher temperatures over NH continents and a stronger polar vortex in the lower stratosphere. We also examined NH summer precipitation responses in the first year after the eruptions and find clear reductions of summer Asian and African monsoon rainfall.

1. Introduction

Volcanic eruptions can have global climate impacts lasting several years. Indeed, large explosive eruptions can inject sulfur gases into the stratosphere, which are then converted to sulfate aerosols [*Robock*, 2000]. These large masses of stratospheric aerosols decrease incoming shortwave (SW) solar radiation, resulting in the well-known cooling of Earth's surface [*Robock and Mao*, 1995; *Robock*, 2000]. Ice core reconstructions have been vital tools for recording volcanism in the distant past [*Gao et al*., 2008; *Crowley et al*., 2008; *Sigl et al*., 2015]. Over the last millennium (defined here as 850–1850 C.E.), the largest eruption identified by ice core records is the 1257 Samalas eruption. In total, *Gao et al*. [2008] identified 12 eruptions in the last millennium that were larger than the most recent and therefore best-observed 1991 eruption of Mount Pinatubo [e.g., *Minnis et al*., 1993; *Stenchikov et al*., 1998]; *Crowley et al*. [2008] identified eight such eruptions. Sulfate aerosols created by sulfur injected into the tropical stratosphere, from where they are transported poleward, are more likely to have a long-lasting global climate impact than those originating from high-latitude eruptions, which tend to remain at high and midlatitudes [*Kravitz and Robock*, 2011; *Timmreck*, 2012; *Toohey et al*., 2016]. Other factors that have an influence on the climate response to volcanic eruptions include season of eruption and injection height [*Toohey et al*., 2011, 2013, 2016].

In addition to reflecting incoming solar radiation, sulfate aerosols absorb solar near-infrared and terrestrial infrared radiation [e.g., *Lacis et al*., 1992; *Stenchikov et al*., 1998]. For tropical volcanic eruptions, this infrared forcing leads to an anomalously warm equatorial lower stratosphere, increasing the equator-to-pole temperature gradient. Volcanic aerosols are also associated with polar stratospheric ozone loss by activation of halogens, which results in a cooling of the polar stratosphere, further increasing the gradient [*Solomon*, 1999; *Stenchikov et al*., 2002; *Muthers et al*., 2014; *Barnes et al*., 2016]. By the thermal wind relation, the anomalous temperature gradient results in stronger westerly winds in the stratosphere.

It is unclear, however, what contribution the enhanced temperature gradient from heating by volcanic aerosols makes to the strengthened stratospheric polar vortex at 60°N [*Stenchikov et al*., 2002; *Toohey et al*., 2014; *Bittner et al*., 2016b]. It has also been proposed that maximum surface cooling in the tropics weakens the meridional temperature gradient in the troposphere, leading to a decrease in upward planetary wave flux and causing a strengthened polar vortex [*Stenchikov et al*., 2002]. On the other hand, observations show an

increased wave flux after large volcanic eruptions [*Graf et al*., 2007]. Recently, modeling studies have resulted in newly proposed mechanisms for the strengthened polar vortex, including increased stratospheric residual circulation and southward deflection of planetary waves [*Toohey et al*., 2014; *Bittner et al*., 2016b]. Despite the uncertainty with regard to the mechanism, the strengthened polar vortex leads to positive temperature anomalies over northern Eurasia and sometimes parts of North America, a response known as "winter warming" [*Robock and Mao*, 1992; *Perlwitz and Graf*, 1995]. Significant cooling has also been observed in the Middle East [*Robock*, 2000].

A strengthened polar vortex has been associated with a positive phase of the North Atlantic Oscillation (NAO) and the Arctic Oscillation (AO), both indices of the wintertime variability of Northern Hemisphere (NH) sea level pressure [*Hurrell*, 1995; *Thompson and Wallace*, 1998; *Shindell et al*., 2004; *Christiansen*, 2008]. A positive phase of the AO is characterized by anomalously low pressure over the pole and anomalously high pressure at midlatitudes; the anomalies change signs in the negative phase. After large tropical volcanic eruptions a positive phase of the AO has been observed for the following one to two winters [*Robock and Mao*, 1992; *Stenchikov et al*., 2002].

In addition to the surface warming response caused by changes in stratospheric temperature and density gradients, circulation changes caused by atmospheric injection of sulfate aerosols by large volcanic eruptions are thought to reduce summer precipitation in Northern Africa and Asia [e.g., *Rotstayn and Lohmann*, 2002; *Oman et al*., 2006; *Iles and Hegerl*, 2015; *Colose et al*., 2016; *Liu et al*., 2016]. For example, the lowest rainfall in the Sahel region of Africa over 1940–1990 occurred in the summers directly following the 1982 El Chichón eruption, suggesting that large tropical eruptions may tend to strengthen droughts in the region [*Robock and Liu*, 1994]. Similar drought conditions were reported across India in the summer after the 1783–1784 Laki eruption in Iceland [*Mooley and Pant*, 1981]. This is caused by a weakening of the Indian and African monsoon due to inhomogeneous cooling of the land and ocean, which decreases the temperature gradient between Europe and Asia and the Pacific and Indian Oceans [*Oman et al*., 2006; *Liu et al*., 2011; *Man et al*., 2012, 2014; *Man and Zhou*, 2014].

Stenchikov et al. [2006], *Driscoll et al*. [2012], and *Charlton-Perez et al*. [2013] showed that current climate models produced imperfect simulations of the surface winter warming response to large volcanic eruptions when examining an average of the first two NH winters following volcanic eruptions between 40°S and 40°N, producing only a slightly strengthened stratospheric vortex, and failing to reproduce observed NH winter temperature responses following volcanic eruptions. *Charlton-Perez et al*. [2013] also showed that results remained largely unchanged whether considering low-top or high-top models. The perceived inability of climate models to produce this dynamical response in past studies has been attributed to several weaknesses in the models, including a simplified treatment of volcanic aerosols and deficiencies in model implementation of the Brewer-Dobson circulation [*Stenchikov et al*., 2006; *Marshall et al*., 2009; *Thomas et al*., 2009; *Driscoll et al*., 2012]. A lack of ozone chemistry in the models has also been thought to contribute to the lack of a dynamical response, though some debates exist with respect to the importance of ozone depletion for the surface winter warming response [*Stenchikov et al*., 2002; *Marshall et al*., 2009]. Still, others have suggested that the models are unable to produce an AO response to large-scale forcing [*Otterå*, 2008; *Driscoll et al*., 2012], though *Stenchikov et al*. [2004], *Shindell et al*. [2004], and *Bittner et al*. [2016a] showed that this might not be the case.

In contrast to earlier studies, *Zambri and Robock* [2016] found that, if looking at just the first winter after large tropical eruptions, most of the Coupled Model Intercomparison Project 5 (CMIP5) [*Taylor et al*., 2012] models can produce a fairly strong surface winter warming. Through analysis of zonal wind anomalies, *Barnes et al*. [2016] and *Bittner et al*. [2016a] similarly found a strengthened polar vortex in the first winter after the largest eruptions in the CMIP5 historical simulations. In addition, previous studies have suggested that the simulated response does not depend on the chosen volcanic forcing data set [*Driscoll et al*., 2012; *Maher et al*., 2015]. On the other hand, others argue that the choice of volcanic forcing can significantly impact model responses [*Schmidt et al*., 2011; *Toohey et al*., 2014].

Bittner et al. [2016a] and *Zambri and Robock* [2016] were able to isolate the surface winter warming and summer monsoon signals by looking at only large (at least as large as 1991 Pinatubo) tropical volcanic eruptions. However, since 1850 there have only been two such eruptions, 1883 Krakatau and 1991 Pinatubo. Here we look at the previous 1000 years and were able to use 10 large volcanic eruptions, so as to extract a clearer

Table 1. Last Millennium Ensemble Models, Volcanic Forcing Data Set Used[a], and Number of Ensemble Members

Model	Volcanic Forcing	Model Resolution (Lat × Lon × Lev)	Number of Ensemble Members
BCC-CSM1-1	GRA	128 × 64 × 26	1
CESM1-CAM5	GRA	144 × 90 × 26	9 all forcing, 5 volcanic only
CCSM4	GRA	288 × 192 × 26	1
CSIRO-Mk3L-1-2	CEA	64 × 56 × 18	1
FGOALS-s2	GRA	128 × 108 × 26	1
GISS-E2-R	CEA, 2×GRA	144 × 90 × 40	3 CEA, 3 2×GRA
HadCM3	CEA	96 × 73 × 19	1
MIROC-ESM	CEA	128 × 64 × 80	1
MPI-ESM-P	CEA	196 × 98 × 47	1
MRI-CGCM3	GRA, interactive	320 × 160 × 48	1

[a]GRA = *Gao et al*. [2008], CEA = *Crowley et al*. [2008].

signal of the volcanic response for the first winter and summer after large eruptions. We restricted our analysis to eruptions between 40°S and 40°N. We examined the Paleoclimate Modeling Intercomparison Project 3 (PMIP3) [*Braconnot et al*., 2012] last millennium (past1000) simulations and the Community Earth System Model Last Millennium Ensemble (CESM-LME) [*Otto-Bliesner et al*., 2016] for 850 to 1850. The past1000 simulations include six simulations of the Goddard Institute for Space Studies E2-R (GISS-E2-R) climate model and single simulations from eight additional modeling groups (Table 1). For the LME we consider a 14-member ensemble, including five runs with volcanic forcing only. This is the first such analysis for PMIP simulations. The models, experiments, and analyses are described in section 2; results are presented in section 3; and in section 4, we present our discussion and conclusions.

2. Methods

After excluding one additional available model simulation that reduced the solar constant to achieve the radiative forcing associated with volcanic eruptions, we analyzed a total of 28 simulations of the period 850–1850 C.E. This includes 14 simulations from the PMIP3 past1000 experiment and 14 from the LME. Six of the 14 past1000 simulations come from the same model, GISS-E2-R, and so we analyze these runs separately. Furthermore, we separate simulations by the volcanic data set by which they were forced. Specifically, of the eight non-GISS past1000 simulations, four used the *Gao et al*. [2008] (GRA) forcing data set, while the other four used the *Crowley et al*. [2008] (CEA) forcing. Of the six GISS-E2-R simulations, three were forced with about twice the prescribed forcing from the GRA data (2×GRA) and three with the CEA forcing. Aside from the GRA forcing being doubled in the GISS-E2-R simulations, the two volcanic forcing data sets also differ in their conversion from sulfate ice core concentrations to aerosol optical depth (AOD). The GRA forcing assumes a linear relationship between total stratospheric aerosol load and global AOD, while CEA provides an estimate of AOD from a 2/3 power scaling for eruptions larger than the 1991 Pinatubo eruption [*Crowley and Unterman*, 2013; *Metzner et al*., 2014]. The GISS simulations also presume the same relationship between AOD and effective radius as in *Sato et al*. [1993], making the aerosol particle sizes proportionally larger for the larger eruptions. In addition, MRI-CGCM3 interactively computes the conversion from SO_2 injection to stratospheric aerosol; this is the only model of the set that uses an interactive scheme. Different events are captured in the two data sets, and common events often have different amplitudes based on the different methods of conversion [*Sigl et al*., 2014]. Thus, we analyze the GRA-forced and CEA-forced simulations separately. All 14 of the CESM-LME simulations used the GRA forcing. Nine of the simulations included all forcings, while the remaining five included only volcanic forcing. We analyze the all-forcing and the volcano-only runs separately. Although five of the six ensembles include all forcings, while the last includes volcanic forcing only, other forcings (e.g., greenhouse gases, ozone, and tropospheric aerosols) were set to preindustrial levels and therefore should not have an impact on the results. Therefore, it is valid to compare the volcano-only simulations with those simulations that have all forcings implemented. Only MIROC-ESM includes an internally generated quasi-biennial oscillation. More information about the individual models can be found in Table 1.

We analyze surface air temperature, zonal mean zonal wind, geopotential height, and mean sea level pressure for the first NH winter (December, January, and February (DJF)) and precipitation for the first NH

Table 2. Volcanic Eruptions Analyzed From the CMIP5/PMIP3 Past1000 Ensemble[a]

Eruption Year (C.E.)	Volcano	Latitude	Stratospheric Sulfate Aerosol Mass (Tg)[b]	Total Sulfate Aerosol Flux (kg km^{-2})
1167[c]	Kirishima	31°N	52.12	10.9
1227	Zaozan	38°N	67.52	51.2
1258	Samalas	8°S	257.91	196.9
1275[c]	Quilotoa	1°S	63.72	10.0
1284	Unidentified	?	54.69	15.1
1452	Kuwae	17°S	137.50	59.1
1600	Huaynaputina	17°S	56.59	45.7
1641[c]	Parker	6°N	51.60	17.6
1673[d]	Gamkonora	1°N	16.13	20.1
1694[d]	Unidentified	?	27.1	28.3
1809	Unidentified	?	53.74	40.6
1815	Tambora	8°S	109.72	84.8
1835[d]	Cosigüina	13°N	40.16	22.7

[a]Eruptions in years without a superscript were analyzed for all runs.
[b]Aerosol mass is from *Gao et al.* [2008]. Aerosol flux is from *Crowley et al.* [2008].
[c]Volcano was used only in GRA-forced runs.
[d]Volcano was used only in CEA-forced runs.

summer (June, July, and August (JJA)) after the 10 largest eruptions between 40°S and 40°N in the 850–1850 C.E. period. While there are common events, there are some events that are captured in one forcing data set but not in the other. Therefore, the 10 volcanic eruptions analyzed are not the same for each set of simulations. The eruptions, the years and latitudes of eruption, the stratospheric sulfate aerosol mass [*Gao et al.*, 2008] and total sulfate aerosol flux [*Crowley et al.*, 2008], and the forcing data set where each eruption appears are listed in Table 2. The choice of restricting analysis to eruptions in the 40°S–40°N band is made because high-latitude eruptions should not in general be expected to produce a positive AO and the associated NH surface warming response [e.g., *Oman et al.*, 2005]. Anomalies are calculated by subtracting the average of the five winters (for surface temperature, zonal mean zonal wind, sea level pressure, and geopotential height) or summers (for precipitation) before each eruption from the first winter or summer after the eruption. Because of the close proximity of the 1809 and 1815 eruptions, we use the same reference period (1804–1808) for these two eruptions. We assess the statistical significance of anomalies at the 95% level using a local two-tailed Student's *t* test, assuming for the multimodel means that each volcano and each model realization represents independent samples.

In addition, we test whether looking at the principal modes of variability yields a response similar to those delivered from the aforementioned analyses. Specifically, the AO index is computed for each ensemble member of each model, and model responses are compared using a superposed epoch analysis of the winter AO for the 10 volcanic eruptions listed in Table 1.

3. Results

3.1. Radiative Effects

We follow the convention of previous studies of using the time series of the anomalies in the top-of-atmosphere (TOA) reflected SW radiation (Figure 1; full 850–1850 time series in Figure S1 in the supporting information) as a rough proxy for the global radiative effect of the volcanic aerosol [*Stenchikov et al.*, 2006; *Driscoll et al.*, 2012]. All of the models perform reasonably consistently with each other and reveal an increase in the reflected SW radiation corresponding to the explosive volcanic eruptions, though some noticeable differences do exist. Differences in reflected SW radiation are more dependent on model choice than on the choice of volcanic forcing. Specifically, the GISS-CEA ensemble simulates larger anomalies in reflected SW radiation than the PMIP-CEA ensemble, and the CESM-LME ensemble simulates larger anomalies than the PMIP-GRA ensemble. On the other hand, for most of the common events (e.g., 1260, 1284, 1809, and 1815), the GRA and CEA forcings elicit similar responses in the CESM-LME and GISS-CEA ensembles. As should be expected, the largest anomalies overall are produced by the 2×GRA GISS-E2-R ensemble. Reflected SW radiation anomalies for this ensemble are approximately 4 times larger than the anomalies in the other single-model ensembles, and these anomalies are scaled by a factor of 0.25 in Figure 1 for comparison with the other ensembles.

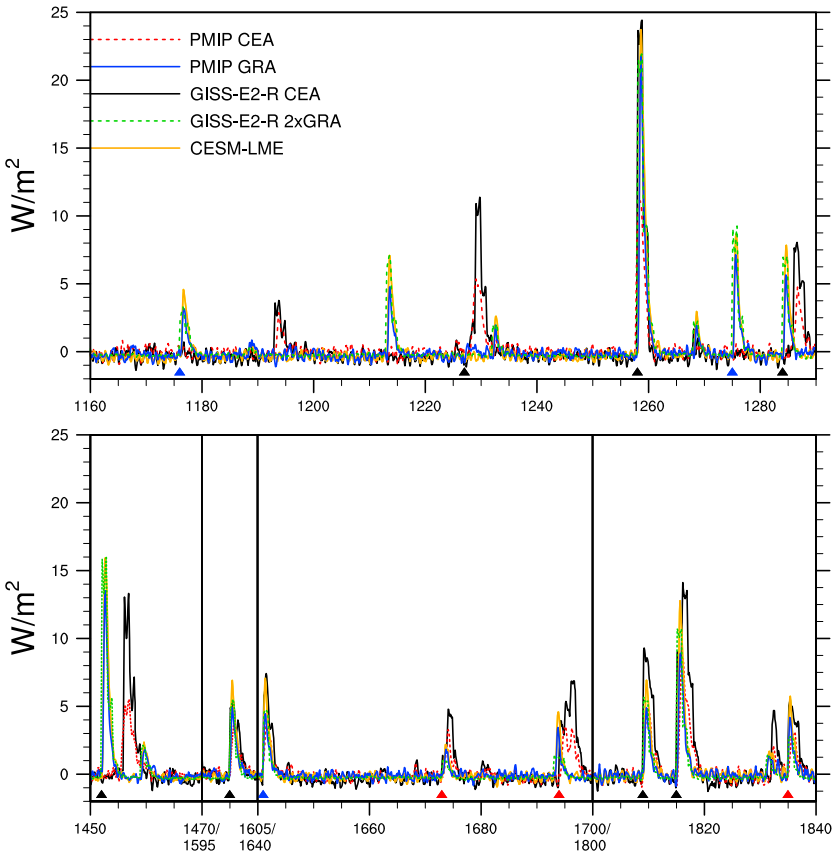

Figure 1. Three-month running means of the anomalies in global-averaged reflected solar flux (W m^{-2}) for selected periods. Results plotted for the six ensembles (Table 1) and represent averages over all the individual realizations for each ensemble. GISS-E2-R 2×GRA anomalies are scaled by a factor of 0.25. The blue, red, and black triangles indicate volcanic eruptions analyzed for the GRA forcing only, the CEA forcing only, and for both forcings, respectively.

In contrast to the radiative cooling demonstrated by anomalies in TOA reflected SW radiation, we measured the anomalous heating forced by the volcanic aerosol in the lower stratosphere by analyzing the anomalies in the detrended 30°S–30°N, 50 hPa temperature. Figure 2 (full 850–1850 time series in Figure S2) shows that, unlike the radiative cooling, which exhibited higher dependence on the model, the variability in stratospheric temperature due to volcanic eruptions is more strongly influenced by the forcing data set chosen. Specifically, the GRA-forced ensembles show significantly larger heating anomalies than the CEA-forced ensembles, including for common events. In this case, the CESM-LME ensembles simulate the largest heating anomalies of the singly forced ensembles. The 2×GRA GISS-E2-R temperature anomalies are approximately 1 to 2 times as large as the other GRA-forced ensembles, depending on the eruption, and anomalies for this ensemble are scaled by a factor of 0.5 in Figure 2. The results in this section indicate that we might expect the weakest surface winter warming response from the CEA-forced ensembles, as the magnitude of lower stratospheric heating in these simulations is affected by the aforementioned 2/3 power scaling.

3.2. Surface Temperature

Figure 3 illustrates the surface air temperature anomalies for the first DJF winter after the 10 volcanic eruptions. The CEA-forced PMIP multimodel average (Figure 3a) shows very little warming over northern Eurasia, with anomalies below 0.5 K. On the other hand, the GRA-forced PMIP multimodel average does simulate significant warming in this region (Figure 3b). In this case, the maximum anomaly is above 1.5 K in northern Europe. The CEA-forced GISS-E2-R runs (Figure 3c) simulate mostly cooling in the NH, with some warming (anomalies less than 1 K and not statistically significant) over northern Europe and Asia. The 2×GRA forcing runs (Figure 3d) simulate significant warming over most of northern Eurasia and northeastern North America, with anomalies almost uniformly above 2 K and reaching above 4 K. All of the models show cooling

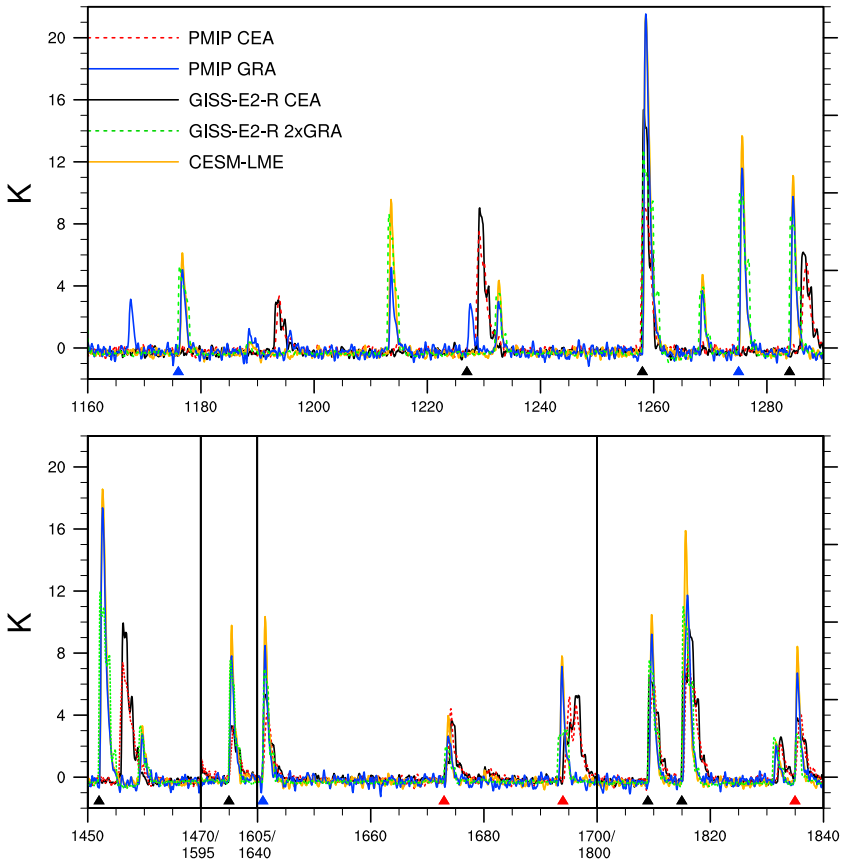

Figure 2. Three-month running means of the 50 hPa temperature anomalies (K) averaged between 30°S and 30°N. Results plotted for the six ensembles (Table 1) and represent averages over all the individual realizations for each ensemble. GISS-E2-R 2×GRA anomalies are scaled by a factor of 0.5. The blue, red, and black triangles indicate volcanic eruptions analyzed for the GRA forcing only, the CEA forcing only, and for both forcings, respectively.

over northern Africa, the Middle East, and the tropics, with anomalies generally being greater in magnitude in the GRA-forced runs. The all-forcing CESM runs reveal significant warming over almost all of northern Europe and Asia, with the maximum anomaly above 2 K (Figure 3e); similar results are seen in the volcano-only runs (Figure 3f). One feature that is unique to the CESM ensemble is warming in the Weddell Sea.

Figure S3 illustrates the individual PMIP model mean responses in the first winter after the eruption. HadCM3 shows warming over eastern Eurasia, although there is also warming over Greenland, which should not in general be expected. MIROC-ESM reveals no warming over Europe, and only a small patch of warming in Southeast Asia. BCC-CSM1-1, MPI-ESM-P, CCSM4, FGOALS-s2, and MRI-CGCM3 all simulate surface winter warming, though only anomalies in MRI-CGCM3 are significant. The lack of statistical significance is due to a combination of a low number of years averaged for each model (10) and the high variability of NH winter [*Bittner et al*., 2016a]. Still, most of the models do simulate surface winter warming over Europe, with several models simulating anomalies above 2 K. Figures 4 and S4 show surface temperature anomalies for the second winter after the eruptions. While surface cooling from the eruptions is still evident, only the doubly forced GISS-E2-R runs (Figure 3d) and MRI-CGCM3 (Figure S4, bottom right), which uses an interactive aerosol scheme, display significant surface winter warming for 2 years after the eruption.

In addition to the warming response over NH landmasses, the impact of volcanic eruptions on the El Niño–Southern Oscillation (ENSO) has been investigated at length, with mixed results. Some studies found a connection between volcanic eruptions and ENSO events [*Mann et al*., 2005; *McGregor and Timmermann*, 2011; *Wahl et al*., 2014; *Maher et al*., 2015; *Stevenson et al*., 2016, 2017; *Le*, 2017; *Predybaylo et al*., 2017], while others found little or no correlation [*Robock et al*., 1995; *Self et al*., 1997; *Ding et al*., 2014]. Figure 3 and the first four panels in Figure 4 show very little ENSO activity in the first two postvolcanic winters, with very little, mostly insignificant, temperature changes in the tropical Pacific. Only in Figures 4e and 4f does significant warming

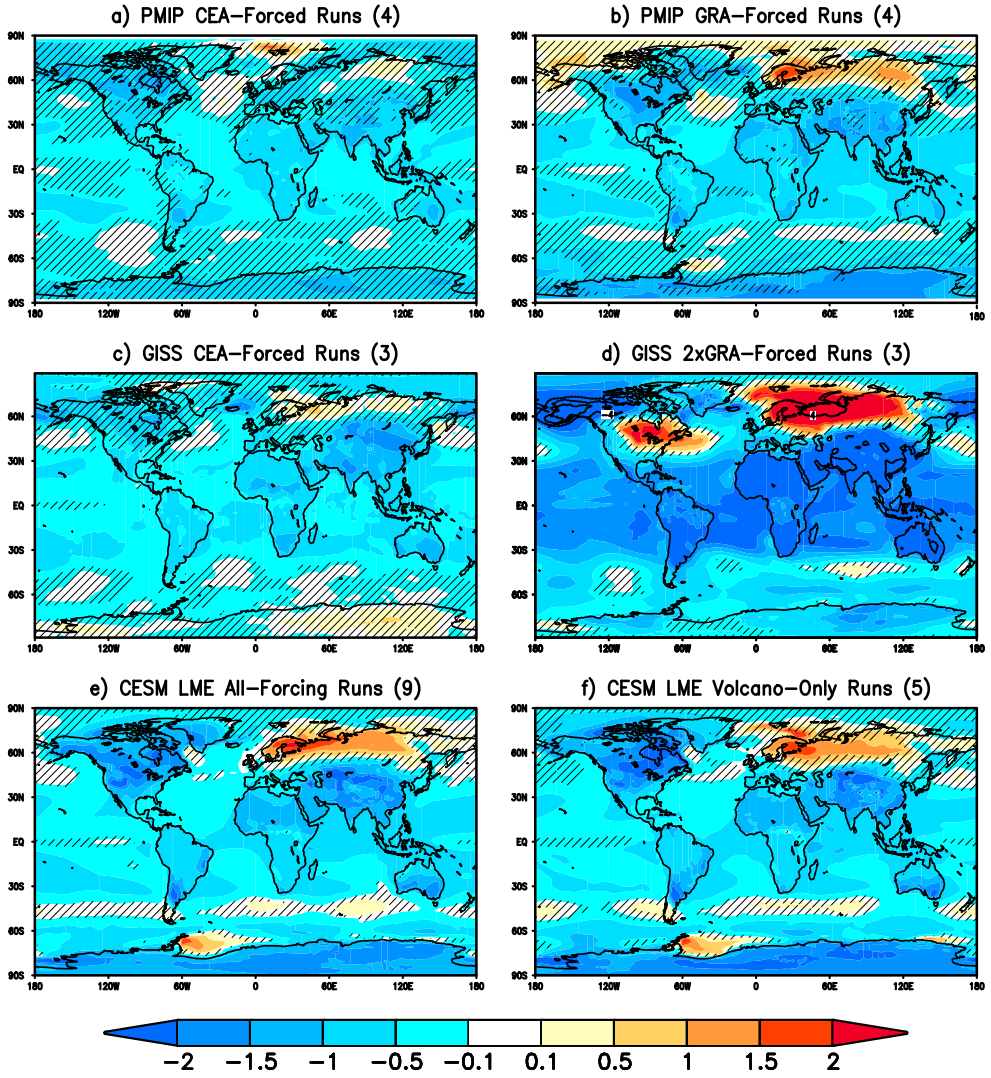

Figure 3. Surface temperature anomalies with respect to the 5 years preceding each eruption (K) for the first winter (DJF) after the 10 largest tropical eruptions spanning 850–1850 (Table 1) for (a) CEA-forced PMIP runs, (b) GRA-forced PMIP runs, (c) CEA-forced GISS-E2-R runs, (d) 2×GRA-forced GISS-E2-R runs, (e) all-forcing CESM-LME runs, and (f) volcano-only CESM-LME runs. Hatching displays areas below 95% significance using a two-tailed *t* test.

over the tropical Pacific Ocean indicate an increased likelihood of the formation of an El Niño after a volcanic eruption. However, this El Niño-like signal is observed only in the second winter and only in the CESM-LME ensembles, in agreement with *Stevenson et al.* [2016]. These results are evidence of the model dependence of this phenomenon, which is further supported by the aforementioned studies, each of which used a different set of models.

3.3. Zonal Wind

Strengthened zonal winds in the midlatitude stratosphere result in a stronger polar vortex, a dynamical response that has been observed after volcanic eruptions in the past [e.g., *Graf et al.*, 2007]. This strengthened polar vortex drives the surface winter warming response, and for this reason, we first analyze the zonal wind anomalies in the different sets of experiments, as one may not expect a response at the surface if the zonal winds are not significantly strengthened. Figure 5 shows the winter zonal mean zonal wind responses to the selected 10 large volcanic eruptions.

Though all ensembles exhibit significantly strengthened westerlies at 60°N, the anomalies vary considerably in magnitude and spatial extent. Specifically, the PMIP CEA-forced multimodel mean (Figure 5a) and the CEA-

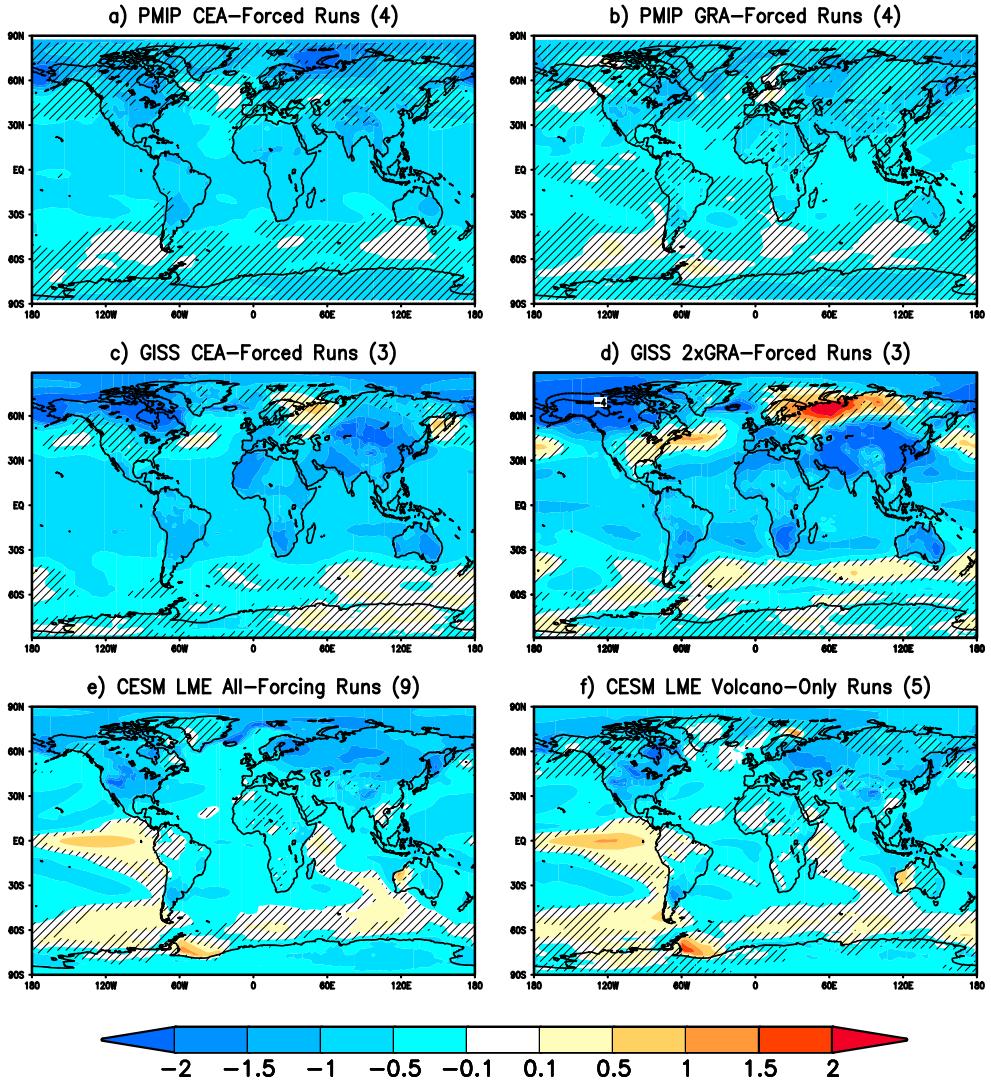

Figure 4. Surface temperature anomalies with respect to the 5 years preceding each eruption (K) for the second winter (DJF) after the 10 largest tropical eruptions spanning 850–1850 (Table 1) for (a) CEA-forced PMIP runs, (b) GRA-forced PMIP runs, (c) CEA-forced GISS-E2-R runs, (d) 2×GRA-forced GISS-E2-R runs, (e) all-forcing CESM-LME runs, and (f) volcano-only CESM-LME runs. Hatching displays areas below 95% significance using a two-tailed *t* test.

forced GISS-E2-R ensemble (Figure 5c) simulate the weakest anomalies, with a maximum strengthening of less than 5 m/s in Figure 5a and less than 3 m/s in Figure 5b. On the other hand, all of the other analyses (Figures 5b and 5d–5f) show stronger anomalies similar to those simulated in previous studies [e.g., *Bittner et al*., 2016a]; that is, these simulations reveal significantly strengthened westerlies in the polar lower stratosphere, with the anomalies changing signs at lower latitudes and altitudes. The PMIP GRA-forced runs (Figure 5b) reach a maximum strengthening above 5 m/s around 60°N in the polar stratosphere, and significant westerly wind anomalies extend down to about 200 hPa. Anomalies in the polar region reach a maximum of 17 m/s and extend to the surface in the 2×GRA-forced GISS simulations (Figure 5d). This extreme case may be expected because of the doubled forcing, but the contrast between Figures 5a and 5b and between Figures 5c and 5d shows that the choice of forcing data set can significantly impact the ability of a model to produce a strengthened polar vortex in response to a low-latitude volcanic eruption, in agreement with past studies [*Toohey et al*., 2014; *Bittner et al*., 2016b]. The ensemble means of the CESM simulations produce almost identical results, both in spatial pattern and magnitude of anomalies. The maximum anomaly is 7 m/s in the polar stratosphere, and the westerly wind anomalies reach about 300 hPa for the all-forcing average (Figure 5e) and 500 hPa for the volcano-only average (Figure 5f).

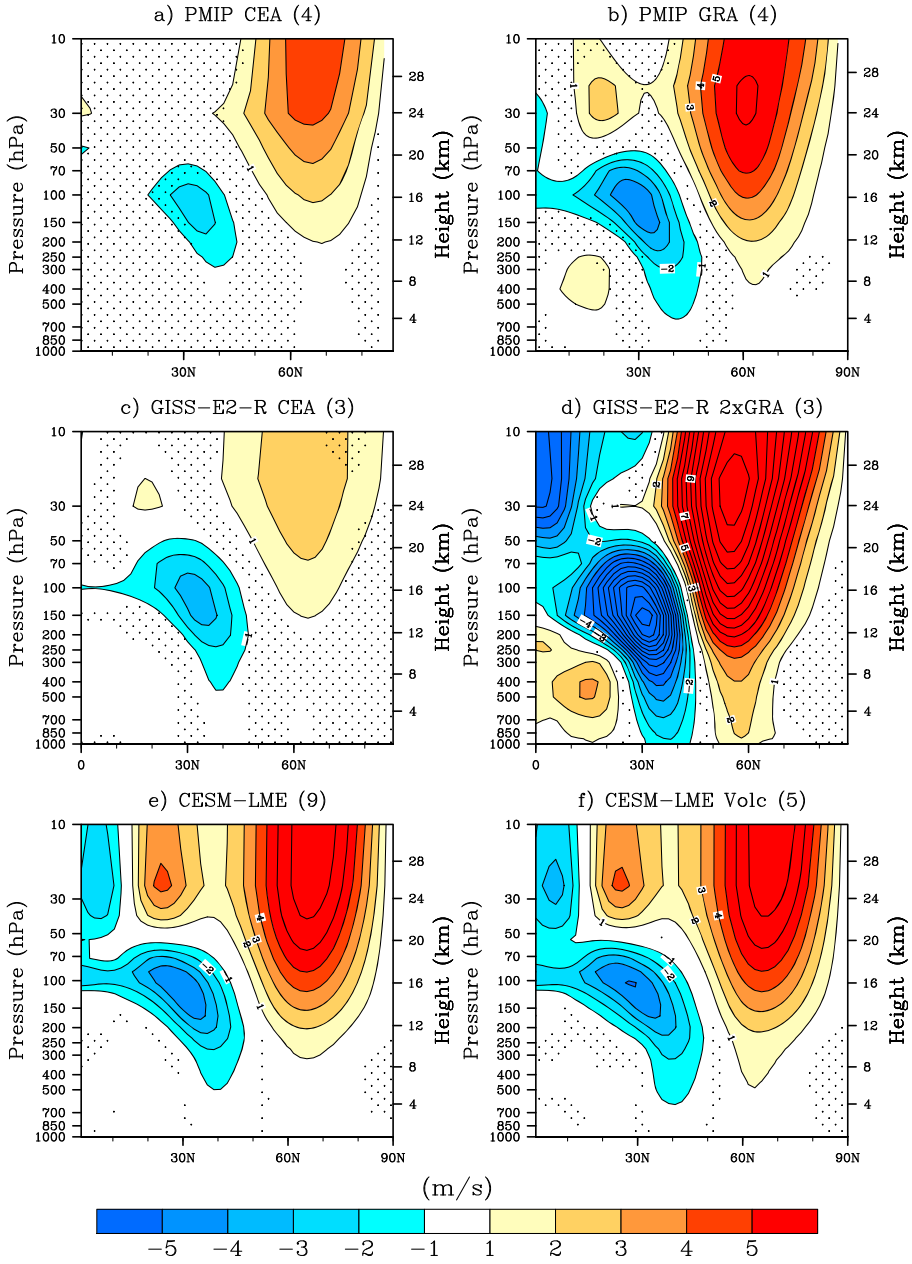

Figure 5. NH zonal mean zonal wind anomalies with respect to the 5 years preceding each eruption (m/s) for the first winter (DJF) after the 10 largest tropical eruptions spanning 850–1850 (Table 1) for (a) CEA-forced PMIP runs, (b) GRA-forced PMIP runs, (c) CEA-forced GISS-E2-R runs, (d) 2×GRA-forced GISS-E2-R runs, (e) all-forcing CESM-LME runs, and (f) volcano-only CESM-LME runs. Contours represent 1 m/s intervals; stippling displays areas below 95% significance using a two-tailed *t* test.

Of course, variability between models also plays a role in the differences seen in Figures 5a and 5b. For this reason, we present in Figure S5 the results for the individual models that make up the two PMIP ensembles. Of the eight models, all but CSIRO-Mk3L-1-2 and BCC-CSM1-1 display significantly strengthened zonal winds in the stratosphere near 60°N. CSIRO-Mk3L-1-2 is the coarsest model, with only 18 vertical levels, which surely contributes to the lack of a response. However, BCC-CSM1-1 has a vertical and horizontal resolution similar to many of the models that do simulate strengthened westerly winds after the eruption. MIROC-ESM and MRI-CGCM3 models, which have the highest vertical resolutions, simulate the largest anomalies in zonal wind. MPI-ESM-P, CCSM4, HadCM3, and FGOALS-s2 also produce strengthened westerlies. Figure S5 illustrates that, on the average, the two ensembles simulate similar responses; the difference in magnitude of response in

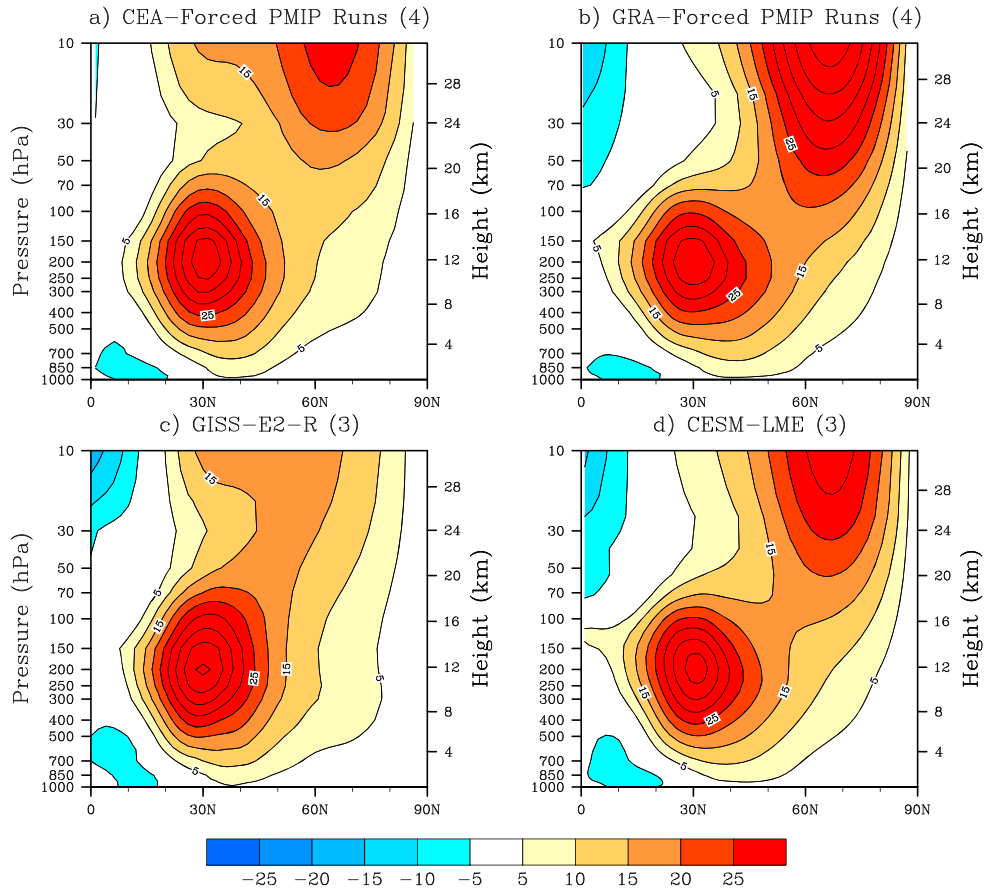

Figure 6. NH DJF zonal mean zonal wind climatology for the period 850–1850 for (a) CEA-forced PMIP ensemble, (b) GRA-forced PMIP ensemble, (c) GISS-E2-R, and (d) CESM-LME. Contours represent 5 m/s intervals.

Figures 5a and 5b is due to the exceedingly strong response from MRI-CGCM3. In addition, while the models with the highest resolutions do simulate the strongest responses, models with similar resolutions yield markedly different responses. Similar to the surface response, MRI-CGCM3, which handles aerosols interactively, shows the strongest response.

Uncertainty in the model results is due to several sources: forcing uncertainty, differences in forcing and model physics, model uncertainty, and internal variability [*Toohey et al*., 2014; *Bittner et al*., 2016a]. The different responses between Figures 5a and 5b and between Figures 5c and 5d are examples of several of these uncertainties. Specifically, Figures 5c and 5d are results from different forcings in the same model, while Figures 5a and 5b are results from different forcings in different models. To further explore model dependence, Figure 6 shows the DJF zonal mean zonal wind for the period 850–1850 for the CEA-forced PMIP models, the GRA-forced PMIP models, GISS-E2-R, and CESM. A comparison of the zonal winds from the different models illustrates that the CEA-forced PMIP models (Figure 6a) and GISS-E2-R (Figure 6c) exhibit weaker mean zonal winds north of 60°N in the stratosphere than do the other models. Results from the individual models (Figure S6) are consistent with this analysis in that the CEA-forced models tend to have weaker zonal wind climatologies than the GRA-forced models. This can, to some extent, explain why two of the ensembles are unable to sufficiently represent zonal wind anomalies in response to stratospheric heating due to volcanic aerosol and why GISS-E2-R requires a very strong forcing to simulate a significant response. However, two of the CEA-forced PMIP models, MIROC-ESM and MPI-ESM-P, which simulate zonal wind climatologies closest to the reanalysis, do simulate substantial changes in zonal wind in response to the volcanic eruptions, as illustrated in Figure S5. In addition, BCC-CSM1-1, which simulates one of the strongest NH winter zonal wind climatologies, exhibits no changes in the polar stratosphere in response to volcanic eruptions. Therefore, the extent to which weaker mean winds can explain the discrepancy in the response between models is limited.

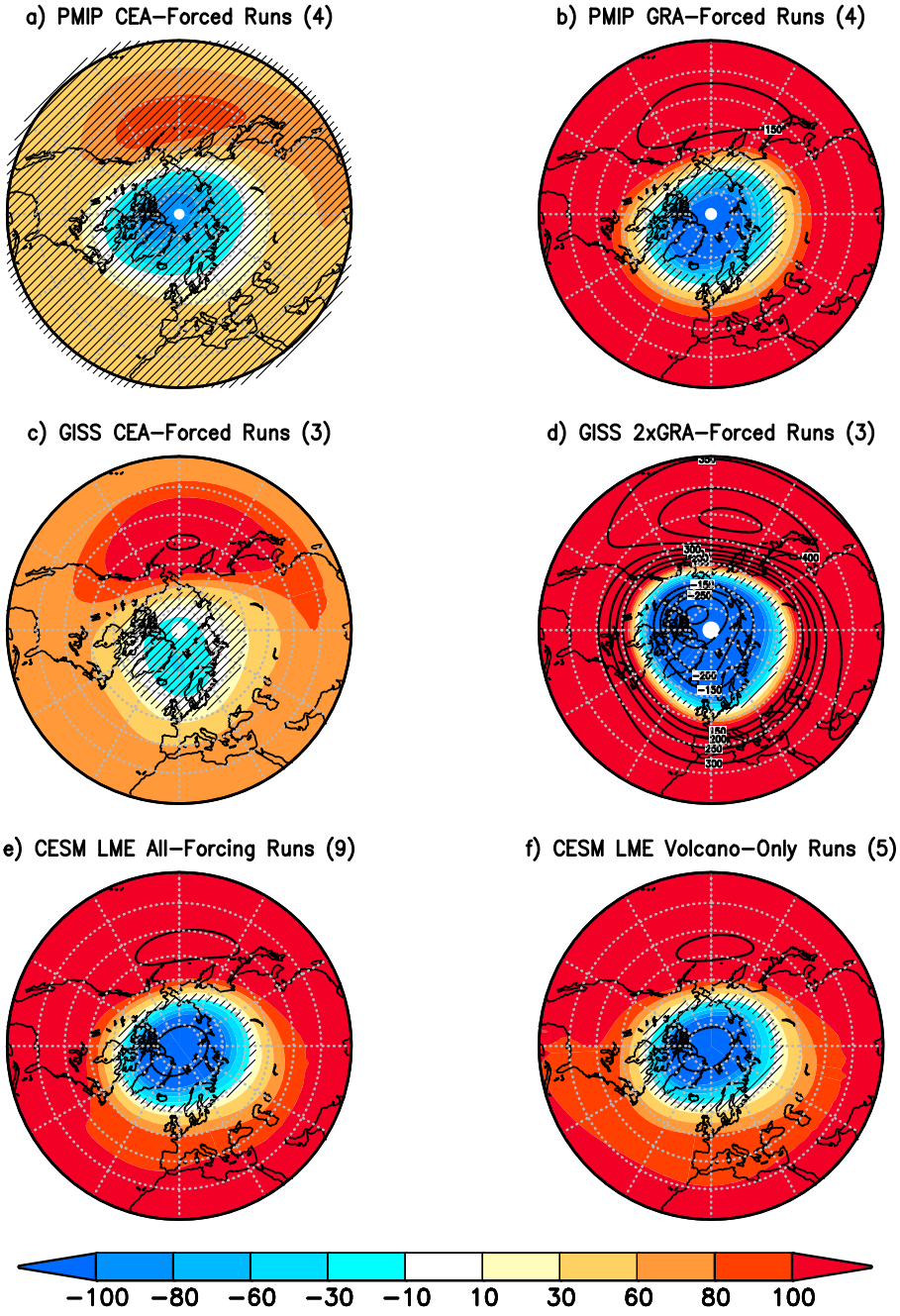

Figure 7. 50 hPa geopotential height anomalies with respect to the 5 years preceding each eruption (m) for the first winter (DJF) after the 10 largest tropical eruptions spanning 850–1850 (Table 1) for (a) CEA-forced PMIP runs, (b) GRA-forced PMIP runs, (c) CEA-forced GISS-E2-R runs, (d) 2×GRA-forced GISS-E2-R runs, (e) all-forcing CESM-LME runs, and (f) volcano-only CESM-LME runs. Hatching displays areas below 95% significance using a two-tailed *t* test. Contours represent 50 m intervals below −100 m and above 100 m.

3.4. Geopotential Height

Several mechanisms have been proposed for the dynamical response that causes a stronger polar vortex after low-latitude volcanic eruptions [*Stenchikov et al.*, 2002; *Driscoll et al.*, 2012; *Toohey et al.*, 2014; *Bittner et al.*, 2016b]. This strengthened and persisting polar vortex can be observed in the 50 hPa geopotential height field and is characterized by negative anomalies near the pole and positive anomalies toward the equator. Figure 7 depicts the 50 hPa geopotential height anomalies for the first winter after the 10 largest eruptions in the six ensembles. Similarly to the results in section 3.3, all ensembles reveal a strengthened

polar vortex, but with anomalies of varying magnitudes. The CEA-forced PMIP runs simulate a strengthened polar vortex with significant negative anomalies near the pole (Figure 7a). The maximum positive and negative anomalies are above 80 m and below −80 m, respectively. The individual PMIP model results (Figure S7) demonstrate that this apparently insignificant anomaly is affected by a disproportionately weak response from a single model (CSIRO-Mk3L-1-2). Indeed, three of the four CEA-forced PMIP models do produce a significantly strengthened polar vortex. The CEA-forced GISS ensemble (Figure 7c) exhibits significant positive anomalies associated with warming by sulfate aerosol. On the other hand, the negative anomalies at the pole are not significant and are almost everywhere above −30 m. The GRA-forced ensembles simulate a much stronger polar vortex, with anomalies exceeding 100 m in the absolute value covering most of the NH (Figures 7b and 7d–7f). Individual model results for the GRA-forced PMIP runs (Figure S7) are similar to those for the CEA-forced models; three of the four models (CCSM4, FGOALS-s2, and MRI-CGCM3) simulate a significantly strengthened polar vortex, while only one model (BCC-CSM1-1) reveals no significant changes. The significant negative anomalies at the pole are in contrast with previous studies, which showed that models could simulate the increase in geopotential height at lower latitudes but largely failed to simulate the deep polar vortex after large tropical volcanic eruptions [*Stenchikov et al*., 2006; *Driscoll et al*., 2012; *Charlton-Perez et al*., 2013; *Toohey et al*., 2014; *Zambri and Robock*, 2016].

3.5. Sea Level Pressure

A strengthened polar vortex has been associated with a positive phase of the AO [*Baldwin and Dunkerton*, 2001; *Gerber et al*., 2012], the first empirical orthogonal function (EOF) of NH winter monthly sea level pressure anomalies, and a positive phase of the AO has been observed for one to two winters following large tropical volcanic eruptions [*Robock and Mao*, 1992; *Thompson and Wallace*, 1998; *Stenchikov et al*., 2002; *Fischer et al*., 2007; *Christiansen*, 2008]. Consistent with observations of recent large tropical volcanic eruptions, all six data sets simulate low pressure over the pole and high pressure at midlatitudes, though only the 2×GRA GISS and the two CESM-LME ensembles simulate a statistically significant positive phase of the AO. The CEA-forced PMIP runs show small changes in sea level pressure consistent with a positive phase of the AO, with a maximum high-pressure anomaly of 2 hPa in the north Pacific and minimum low-pressure anomaly of −2 hPa over the pole (Figure 8a). However, the weak anomalies are not statistically significant and therefore do not indicate a robust tendency toward a positive AO in these models. The individual model responses (Figure S8) further illustrate the difference in responses in the stratosphere and at the surface. Specifically, in contrast to zonal mean zonal wind and geopotential height anomalies, only one of the four CEA-forced PMIP models (MPI-ESM-P) simulates a pattern of sea level pressure anomalies in line with a positive AO, with anomalies above 2 hPa in the absolute value.

The GRA-forced PMIP runs exhibit a more well-defined AO pattern, with positive anomalies spanning the midlatitudes and significant negative anomalies below −2 hPa near the pole (Figure 8b). Figure S5 further illustrates that three of the four GRA-forced PMIP models (CCSM4, FGOALS-s2, and MRI-CGCM3) do show a tendency toward a positive AO in the winter after a large eruption, though only CCSM4 and MRI-CGCM3 simulate a strong enough response for anomalies to be considered statistically significant and overcome the high variability of the winter season. The CEA-forced GISS runs (Figure 8c) show a tendency toward a positive AO, with significant positive anomalies over Eurasia and the North Atlantic, but the low-pressure anomalies over the pole are weak and not significant, and high pressure is not simulated over North America. The 2×GRA forcing GISS runs (Figure 8d) simulate a strong positive AO the first winter after the eruptions, with significant negative pressure anomalies below −6 hPa over the pole, and anomalously high pressure at midlatitudes, especially over the North Atlantic region. The CESM ensembles exhibit similar patterns, with significant anomalies below −2 hPa at the pole and above 2 hPa at midlatitudes, specifically over the north Pacific (Figures 8e and 8f). One notable difference between these results is that the anomalies over the north Atlantic in the all-forcing ensemble are comparatively weaker than those in the volcano-only ensemble.

We also computed the AO index, whose signature over the Atlantic is similar to that of the NAO [*Hurrell*, 1995]. The AO index is computed for each ensemble member of each model. We first compute the first EOF of the monthly winter (DJF) mean sea level pressure anomalies north of 20°N for the period 850–1850. Each data point is weighted by the square root of the grid area it represents, consistent with *Christiansen* [2008] and *Driscoll et al*. [2012]. The seasonal winter AO index is defined as the principal

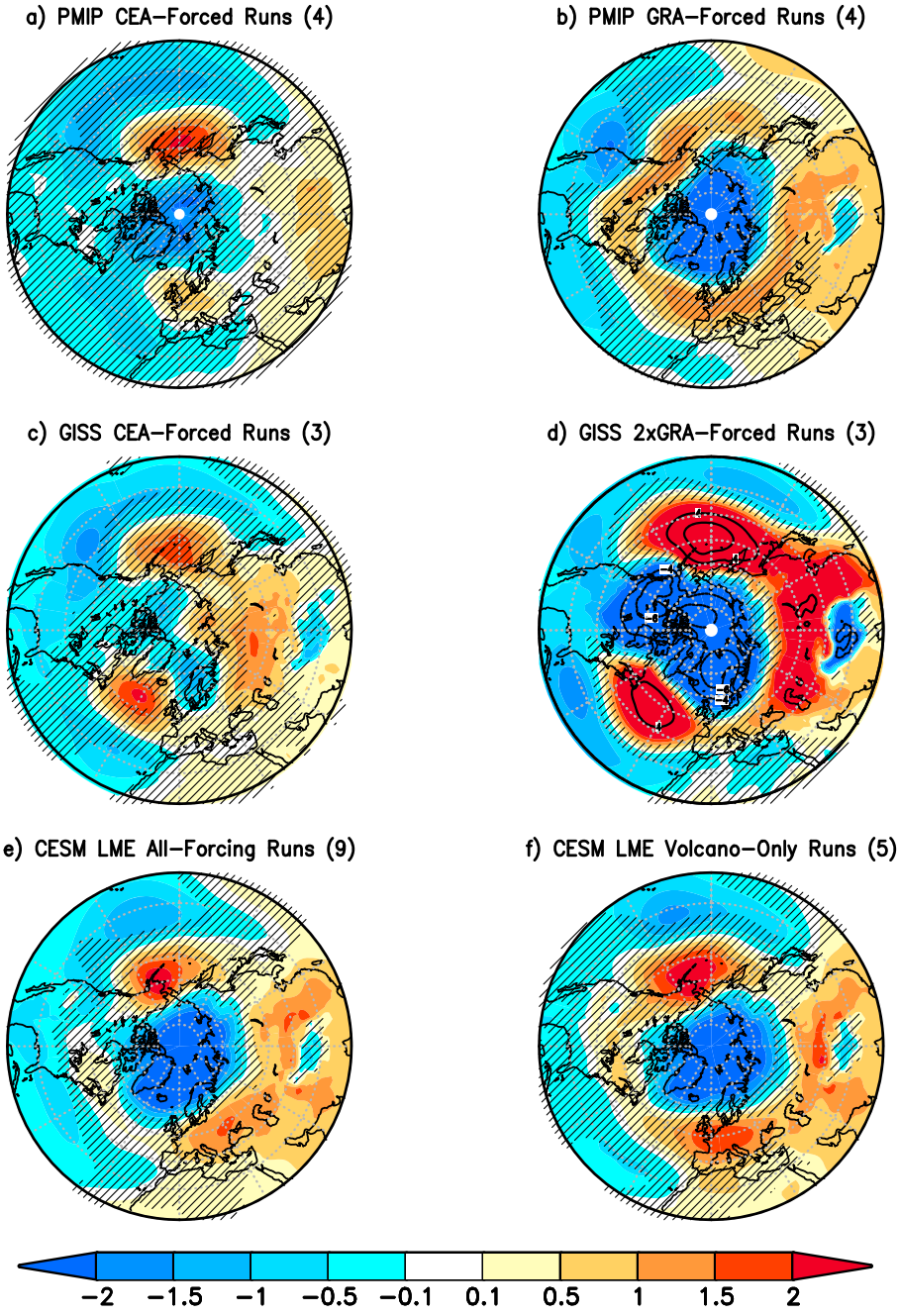

Figure 8. Sea level pressure anomalies with respect to the 5 years preceding each eruption (hPa) for the first winter (DJF) after the 10 largest tropical eruptions spanning 850–1850 (Table 1) for (a) CEA-forced PMIP runs, (b) GRA-forced PMIP runs, (c) CEA-forced GISS-E2-R runs, (d) 2×GRA-forced GISS-E2-R runs, (e) all-forcing CESM-LME runs, and (f) volcano-only CESM-LME runs. Hatching displays areas below 95% significance using a two-tailed *t* test. Contours represent 2 hPa intervals below −2 hPa and above 2 hPa.

component of the monthly anomalies of sea level pressure projected onto the first EOF and normalized to unit variance. Figure 9 shows the EOF pattern for each model.

We compare the model responses using a superposed epoch analysis of the winter AO for the 10 volcanic eruptions listed in Table 1. We take the winters in the 10 years neighboring the first winter before each eruption (5 years before and 5 years after) and generate an "eruption matrix," whose rows represent each eruption event. The rows are then averaged to obtain the epoch composite of 11 years, from winter in year −5 to winter

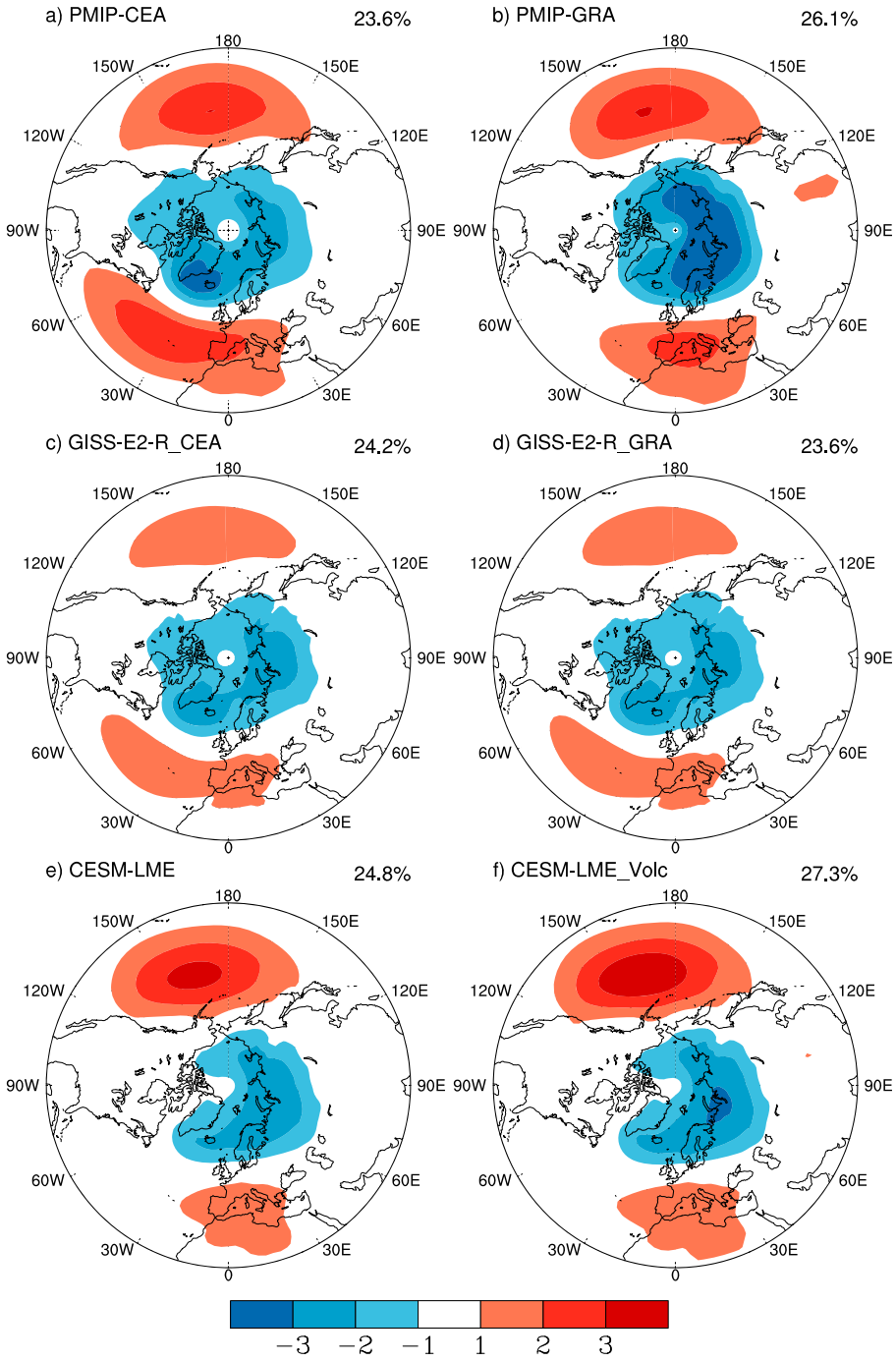

Figure 9. Leading EOF of the monthly winter (DJF) mean sea level pressure anomaly over the north of 20°N for each ensemble mean over the period 850–1850. EOF values are expressed as hPa. In the top right corner of each plot is indicated the percentage of variance explained by the first EOF.

in year +5 with year 1 the first winter after an eruption. The statistical significance of the epoch analysis is estimated using a bootstrap method, by which we generate a "random eruption matrix" by reshuffling with replacement the elements of each row and average the rows into a new epoch composite. The procedure is repeated 5000 times obtaining a distribution of AO values for each lag of the epoch composite. We compare the level of the AO index for each year of the composite with the 5%–95% and 1%–99% percentile levels of the bootstrap distribution.

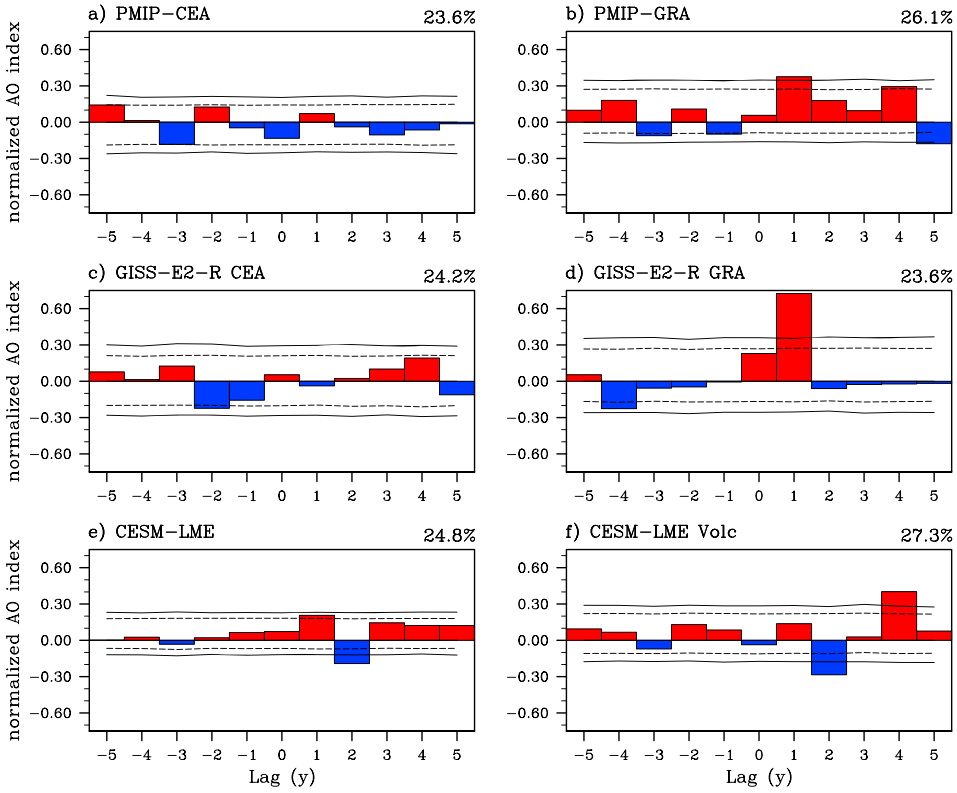

Figure 10. Superposed epoch analysis for the winter (DJF) AO index for the six ensembles for the 10 eruptions listed in Table 2. The average over 10 volcanic eruptions is shown at different lag time. Lag 1 indicates the first winter after a volcanic eruption. In the top right corner of each plot is indicated the percentage of variance explained by the first EOF. The dotted horizontal lines show the 5th and 95th percentiles of the bootstrap distribution; the solid horizontal lines show the 1st and 99th percentiles.

Figure 10 illustrates the results of the superposed epoch analysis. Among the six ensembles analyzed in this study, a positive AO signal at lag 1 is observed for all ensembles but the CEA-forced GISS-E2-R ensemble (Figure 10c). However, only PMIP-GRA (Figure 10b), GISS-E2-R 2×GRA (Figure 10d), and CESM-LME (Figure 10e) reveal a statistically significant positive AO at lag 1. Indeed, the observed positive AO at lag 1 in Figures 10a and 10f may be spurious, since the CEA-forced PMIP runs produce a significant positive AO at lag −2 (Figure 10a) and the CESM-LME Volc ensemble yields a significant positive AO at lag 4. In fact, three of the six ensembles show a statistically significant positive AO at lag 4; this, too, appears to be deceptive since none of the eruptions were separated by fewer than 6 years.

3.6. Summer Monsoon

After a large, explosive volcanic eruption, the decrease in radiation at the surface cools land preferentially to the ocean. This causes a reduction in land-ocean temperature gradients, thereby decreasing monsoon circulation [e.g., *Man et al*., 2012, 2014; *Man and Zhou*, 2014]. Most of these models were evaluated by *Tilmes et al*. [2013], who found that they do a good job of simulating the current regional monsoon systems. Historical accounts and previous studies support the idea that large tropical eruptions reduce summer precipitation in northern Africa and Asia and may tend to strengthen droughts in the region [*Oman et al*., 2006; *Iles and Hegerl*, 2014]. In addition, *Colose et al*. [2016] showed that the GRA-forced GISS-E2-R and CESM ensembles simulate a significant decrease in tropical precipitation after tropical volcanic eruptions.

Figure 11 illustrates the global precipitation responses in the first summer (JJA) after the selected volcanic eruptions. The CEA-forced PMIP runs simulate reductions below −0.5 mm/d over Africa, but the response over Asia is less homogeneous, with both positive and negative anomalies occurring there (Figure 11a). In contrast, there are significant reductions in precipitation below −1 mm/d over much of Asia in the GRA-forced PMIP ensemble (Figure 11b). In agreement with Figure 11a, the GRA-forced runs reveal a similar

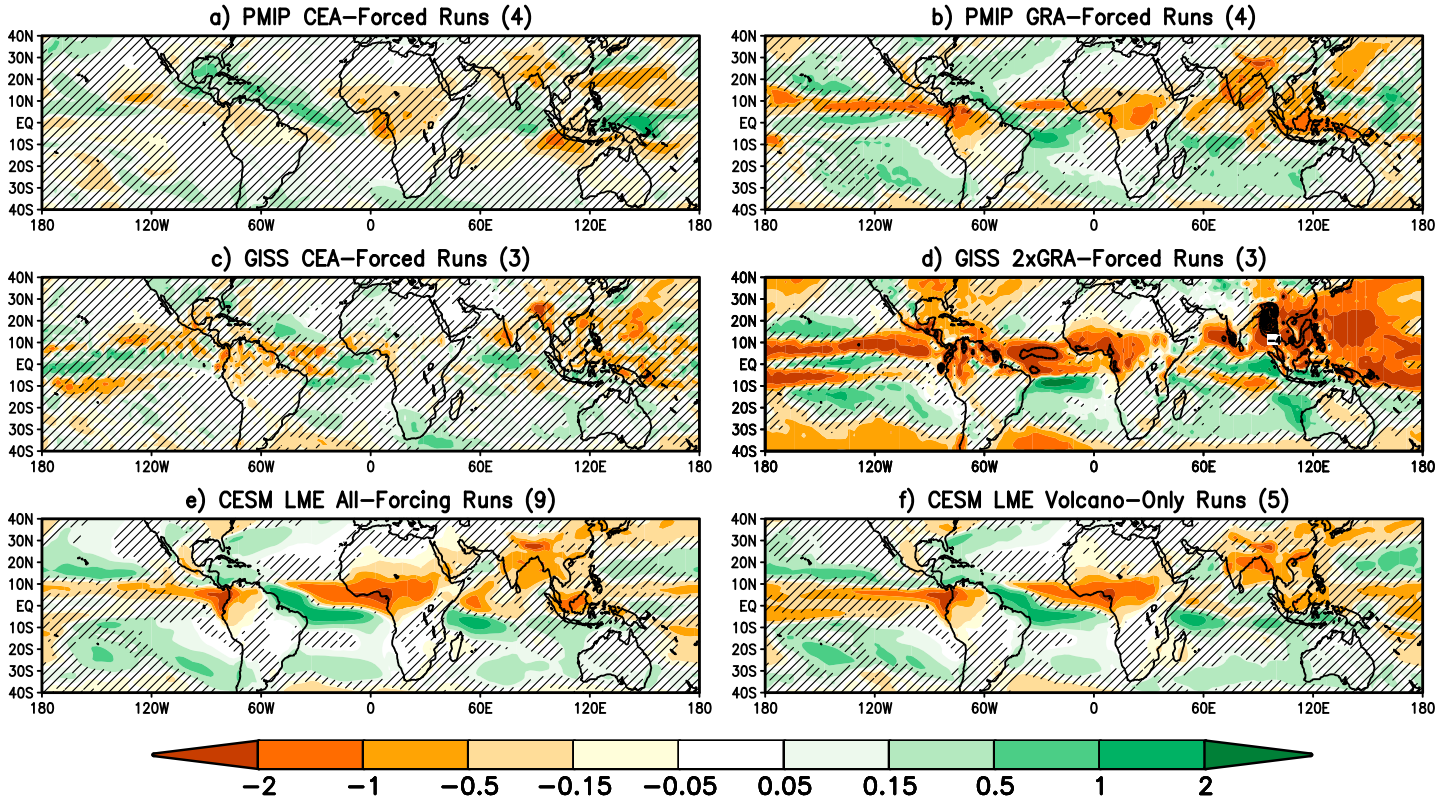

Figure 11. Precipitation anomalies with respect to the 5 years preceding each eruption (mm/d) for the first summer (JJA) after the 10 largest tropical eruptions spanning 850–1850 (Table 1) for (a) CEA-forced PMIP runs, (b) GRA-forced PMIP runs, (c) CEA-forced GISS-E2-R runs, (d) 2×GRA-forced GISS-E2-R runs, (e) all-forcing CESM-LME runs, and (f) volcano-only CESM-LME runs. Hatching displays areas below 95% significance using a two-tailed *t* test.

reduction of precipitation over the Sahel region of Africa, though anomalies in this case are significant and generally larger in magnitude. The CEA forced GISS-E2-R runs (Figure 11c) exhibit reductions in precipitation the Sahel and monsoon Asia, but the anomalies tend to be nonuniform and less than 0.5 mm/d in these regions. On the other hand, the 2×GRA forced GISS-E2-R runs (Figure 11d) simulate significant reductions of rainfall over the Sahel region, India, and most of the Western Pacific Ocean—including much of the maritime continent—with anomalies below −2 mm/d in all three regions. The CESM ensembles (Figures 11e and 11f) indicate reductions in tropical precipitation similar to those in the GRA-forced PMIP ensemble. Specifically, both Figures 11e and 11f exhibit significant reductions in precipitation over much of South and East Asia. Significant reductions are also simulated in the Sahel region of Africa, with reductions below −1 mm/d in much of the region.

Five of the eight PMIP model means (Figure S9) exhibit significant reductions in precipitation over the Sahel region; MIROC-ESM, CSIRO-Mk3L-1-2, and BCC-CSM1-1 do not reveal significant changes, with anomalies both positive and negative there. Responses in Asia are less homogeneous, though all models but MIROC-ESM and CSIRO-Mk3L-1-2 simulate significant reductions in precipitation over parts of India and China.

The results presented here are consistent with previous studies that show reductions in tropical precipitation for the first two boreal summers after large volcanic eruptions [*Iles and Hegerl*, 2014, 2015; *Colose et al*., 2016; *Liu et al*., 2016] and, more specifically, reductions in precipitation in the East Asian monsoon region after large volcanic eruptions [*Liu et al*., 2011; *Man et al*., 2012, 2014; *Man and Zhou*, 2014]. Composite results for the second posteruption summer (not shown) are similar to Figure 11, except that several of the ensembles show a change in the sign of precipitation anomalies over the Sahel.

4. Discussion and Conclusions

Studies in the past have concluded that current global climate models do an imperfect job of reproducing circulation changes and the associated NH warming response during winters after large tropical volcanic

eruptions [*Stenchikov et al*., 2006; *Driscoll et al*., 2012; *Charlton-Perez et al*., 2013]. More recently, *Toohey et al*. [2014] and *Bittner et al*. [2016b] showed that the Max Planck Institute Earth System Model [MPI-ESM; *Giorgetta et al*., 2013] is capable of simulating a strengthened polar vortex in response to a volcanic eruption and that the response is strongly dependent on the forcing chosen and requires a very strong forcing to overcome the high variability of the stratosphere during NH winter. In addition, *Bittner et al*. [2016a] and *Zambri and Robock* [2016] showed that most of the CMIP5 models can, in fact, reproduce this dynamical response in the first winter after an eruption. Both studies used only the two largest tropical eruptions of the historical ensemble period (1850–2005 C.E.), and both found a significantly weaker signal when including smaller eruptions. Here we analyzed the last millennium period, during which there were many more large eruptions than in the historical period analyzed previously. Due to the high variability of the NH stratosphere, it is important to analyze a large number of eruptions and/or simulations [*Toohey et al*., 2014; *Bittner et al*., 2016a, 2016b].

The CESM-LME runs clearly simulate a significantly strengthened polar vortex and a positive AO, both in the all-forcing runs and the volcano-only runs. The GISS-E2-R model produces intense and significant surface winter warming and summer monsoon reduction after volcanic eruptions with the 2×GRA forcing but produces a much weaker and mostly insignificant signal with the CEA forcing. While a large response might be expected due to the large forcing, this analysis demonstrates that differences between forcing data sets play a large role in the model response to volcanic eruptions, which is in agreement with past studies [*Toohey et al*., 2014; *Bittner et al*., 2016b]. Similarly to the GISS-E2-R ensembles, the model responses vary greatly between the CEA-forced and GRA-forced PMIP3 ensembles. While this can certainly be attributed in part to the different forcing data sets used, analysis of the individual model results illustrates that differences between models also have a large influence. For example, the weakest response in all fields was simulated by CSIRO-Mk3L-1-2, a CEA-forced model. However, this is also the model with the lowest horizontal and vertical resolution of all models analyzed (Table 1). On the other hand, the largest response was simulated by MRI-CGCM3, a GRA-forced model. MRI-CGCM3 has the highest horizontal resolution and second-highest vertical resolution of the set and handles volcanic aerosols interactively. Therefore, it should be expected that CSIRO-Mk3L-1-2 would simulate a weak response even to a strong volcanic forcing and MRI-CGCM3 a strong response to a weaker forcing. Comparison of the MPI-ESM-P response (higher resolution, CEA forcing) with the BCC-CSM1-1 response (lower resolution, stronger GRA forcing) is further evidence of the primary importance of model resolution.

Similarly to the results shown by *Toohey et al*. [2014] and *Bittner et al*. [2016b] with the MPI-ESM, we have found that climate models can produce a strengthened polar vortex and surface warming in the first Northern Hemisphere winter after large volcanic eruptions, provided that a sufficiently strong volcanic forcing is considered. While we would not expect climate models on average to exactly simulate the observed response, which includes random variability, these results reaffirm that state-of-the-art climate models in general can simulate realistic responses to large volcanic eruptions. Furthermore, these last millennium ensembles have provided a clearer look at the role of model and forcing dependence on the simulated climate response. These results are important for diagnosing problems with and improving model simulations of volcanic eruptions, as well as for prescribing a single, standard volcanic forcing data set in the future. The upcoming Volcanic Model Intercomparison Project [*Zanchettin et al*., 2016] will use the 1815 Tambora eruption as a standard experiment to force new climate models as part of CMIP6, to continue to improve the simulation of the climate response to volcanic eruptions.

Acknowledgments
This work is supported by the National Science Foundation grant AGS-1430051. The authors thank the Centre for Environmental Data Analysis (http://ceda.ac.uk) for making the CMIP5/PMIP3 output available; Bette Otto-Bliesner and the National Center for Atmospheric Research for making the LME data available; the reviewers for their helpful comments, which improved the manuscript; and the Volcanic Impacts on Climate and Society working group for valuable discussions. A.N.L. thanks NASA GISS for institutional support.

References

Baldwin, M. P., and T. J. Dunkerton (2001), Stratospheric harbingers of anomalous weather regimes, *Science*, *294*(5542), 581–584, doi:10.1126/science.1063315.

Barnes, E., S. Solomon, and L. Polvani (2016), Robust wind and precipitation responses to the Mount Pinatubo eruption, as simulated in the CMIP5 models, *J. Clim.*, *29*, 4763–4778, doi:10.1175/JCLI-D-15-0658.1.

Bittner, M., H. Schmidt, C. Timmreck, and F. Sienz (2016a), Using a large ensemble of simulations to assess the Northern Hemisphere stratospheric dynamical response to tropical volcanic eruptions and its uncertainty, *Geophys. Res. Lett.*, *43*, 9324–9332, doi:10.1002/2016GL070587.

Bittner, M., C. Timmreck, H. Schmidt, M. Toohey, and K. Krüger (2016b), The impact of wave-mean flow interaction on the Northern Hemisphere polar vortex after tropical volcanic eruptions, *J. Geophys. Res. Atmos.*, *121*, 5281–5297, doi:10.1002/2015JD024603.

Braconnot, P., S. P. Harrison, M. Kageyama, P. J. Bartlein, V. Masson-Delmotte, A. Abe-Ouchi, B. Otto-Bliesner, and Y. Zhao (2012), Evaluation of climate models using palaeoclimatic data, *Nat. Clim. Change*, *2*, 417–424, doi:10.1038/nclimate1456.

Charlton-Perez, A. J., et al. (2013), On the lack of stratospheric dynamical variability in low-top versions of the CMIP5 models, *J. Geophys. Res. Atmos.*, *118*, 2494–2505, doi:10.1002/jgrd.50125.

Christiansen, B. (2008), Volcanic eruptions, large-scale modes in the Northern Hemisphere, and the El Niño–Southern Oscillation, *J. Clim.*, *21*, 910–922.
Colose, C. M., A. N. LeGrande, and M. Vuille (2016), Hemispherically asymmetric volcanic forcing of tropical hydroclimate during the last millennium, *Earth Syst. Dyn.*, *7*, 681–696, doi:10.5194/esd-7-681-2016.
Crowley, T. J., and M. B. Unterman (2013), Technical details concerning development of a 1200 yr proxy index for global volcanism, *Earth Syst. Sci. Data*, *5*, 187–197, doi:10.5194/essd-5-187-2013.
Crowley, T. J., G. Zielinski, B. Vinther, R. Udisti, K. Kreutz, J. Cole-Dai, and E. Castellano (2008), Volcanism and the Little Ice Age, *PAGES News*, *16*, 22–23.
Ding, Y., J. A. Carton, G. A. Chepurin, G. Stenchikov, A. Robock, L. T. Sentman, and J. P. Krasting (2014), Ocean response to volcanic eruptions in Coupled Model Intercomparison Project 5 simulations, *J. Geophys. Res. Oceans*, *119*, 5622–5637, doi:10.1002/2013JC009780.
Driscoll, S., A. Bozzo, L. J. Gray, A. Robock, and G. Stenchikov (2012), Coupled Model Intercomparison Project 5 (CMIP5) simulations of climate following volcanic eruptions, *J. Geophys. Res.*, *117*, D17105, doi:10.1029/2012JD017607.
Fischer, E. M., J. Luterbacher, E. Zorita, S. F. B. Tett, C. Casty, and H. Wanner (2007), European climate response to tropical volcanic eruptions over the last half millennium, *Geophys. Res. Lett.*, *34*, L05707, doi:10.1029/2006GL027992.
Gao, C., A. Robock, and C. Ammann (2008), Volcanic forcing of climate over the last 1500 years: An improved ice core-based index for climate models, *J. Geophys. Res.*, *113*, D23111, doi:10.1029/2008JD010239.
Gerber, E. P., et al. (2012), Assessing and understanding the impact of stratospheric dynamics and variability on the Earth system, *Bull. Am. Meteorol. Soc.*, *93*(6), 845–859, doi:10.1175/BAMS-D-11-00145.1.
Giorgetta, M. A., et al. (2013), Climate and carbon cycle changes from 1850 to 2100 in MPI-ESM simulations for the Coupled Model Intercomparison Project Phase 5, *J. Adv. Model. Earth Syst.*, *5*, 572–597, doi:10.1002/jame.20038.
Graf, H.-F., Q. Li, and M. A. Giorgetta (2007), Volcanic effects on climate: Revisiting the mechanisms, *Atmos. Chem. Phys.*, *7*(17), 4503–4511, doi:10.5194/acp-7-4503-2007.
Hurrell, J. W. (1995), Decadal trends in the North Atlantic Oscillation: Regional temperatures and precipitation, *Science*, *269*, 676–679.
Iles, C. E., and G. C. Hegerl (2014), The global precipitation response to volcanic eruptions in the CMIP5 models, *Environ. Res. Lett.*, *9*, doi:10.1088/1748-9326/9/10/104012.
Iles, C. E., and G. C. Hegerl (2015), Systematic change in global patterns of streamflow following volcanic eruptions, *Nat. Geosci.*, *8*, 838–842, doi:10.1038/ngeo2545.
Kravitz, B., and A. Robock (2011), Climate effects of high-latitude volcanic eruptions: Role of the time of year, *J. Geophys. Res.*, *116*, D01105, doi:10.1029/2010JD014448.
Lacis, A., J. Hansen, and M. Sato (1992), Climate forcing by stratospheric aerosols, *Geophys. Res. Lett.*, *19*, 1607–1610, doi:10.1029/92GL01620.
Le, T. (2017), ENSO response to external forcing in CMIP5 simulations of the last millennium, *Global Planet. Change*, *148*, 105–112.
Liu, J., B. Wang, H. Wang, X. Kuang, and R. Ti (2011), Forced response of the East Asian summer rainfall over the past millennium: Results from a coupled model simulation, *Clim. Dyn.*, *36*, 323–336, doi:10.1007/s00382-009-0693-6.
Liu, F., J. Chai, B. Wang, J. Liu, X. Zhang, and Z. Wang (2016), Global monsoon precipitation responses to large volcanic eruptions, *Sci. Rep.*, *6*, 24331, doi:10.1038/srep24331.
Maher, N., S. McGregor, M. H. England, and A. Sen Gupta (2015), Effects of volcanism on tropical variability, *Geophys. Res. Lett.*, *42*, 6024–6033, doi:10.1002/2015GL064751.
Man, W., and T. Zhou (2014), Response of the East Asian summer monsoon to large volcanic eruptions during the last millennium, *Chin. Sci. Bull.*, *59*(31), 4123–4129, doi:10.1007/s11434-014-0404-5.
Man, W., T. Zhou, and J. Jungclaus (2012), Simulation of the East Asian summer monsoon during the last millennium with the MPI Earth System Model, *J. Clim.*, *25*(22), 7852–7866, doi:10.1175/JCLI-D-11-00462.1.
Man, W., T. Zhou, and J. Jungclaus (2014), Effects of large volcanic eruptions on global summer climate and East Asian monsoon changes during the last millennium: Analysis of MPI-ESM simulations, *J. Clim.*, *27*, 7394–7409, doi:10.1175/JCLI-D-13-00739.1.
Mann, M. E., M. A. Cane, S. E. Zebiak, and A. Clement (2005), Volcanic and solar forcing of the tropical Pacific over the past 1000 years, *J. Clim.*, *18*(3), 447–456.
Marshall, A. G., A. A. Scaife, and S. Ineson (2009), Enhanced seasonal prediction of European winter warming following volcanic eruptions, *J. Clim.*, *22*(23), 6168–6180, doi:10.1175/2009JCLI3145.1.
McGregor, S., and A. Timmermann (2011), The effect of explosive tropical volcanism on ENSO, *J. Clim.*, *24*(8), 2178–2191.
Metzner, D., S. Kutterolf, M. Toohey, C. Timmreck, U. Neimeier, A. Freundt, and K. Krüger (2014), Radiative forcing and climate impact resulting from SO_2 injections based on a 200,000-year record of Plinian eruptions along the Central American Volcanic Arc, *Int. J. Earth Sci.*, *103*, 2063–2079, doi:10.1007/s00531-012-0814-z.
Minnis, P., E. Harrison, L. Stowe, G. Gibson, F. Denn, D. Doelling, and W. Smith (1993), Radiative climate forcing by the Mount Pinatubo eruption, *Science*, *259*, 1411–1415.
Mooley, D. A., and G. B. Pant (1981), Droughts in India over the last 200 years, their socio-economic impacts and remedial measures for them, in *Climate and History: Studies in Past Climates and Their Impact on Man*, edited by T. M. L. Wigley, M. J. Ingram, and G. Farmer, pp. 465–478 , Cambridge Univ. Press, New York.
Muthers, S., et al. (2014), Northern hemispheric winter warming pattern after tropical volcanic eruptions: Sensitivity to the ozone climatology, *J. Geophys. Res. Atmos.*, *119*, 1340–1355, doi:10.1002/2013JD020138.
Oman, L., A. Robock, G. L. Stenchikov, G. A. Schmidt, and R. Ruedy (2005), Climatic response to high-latitude volcanic eruptions, *J. Geophys. Res.*, *110*, D13103, doi:10.1029/2004JD005487.
Oman, L., A. Robock, G. L. Stenchikov, and T. Thordarson (2006), High-latitude eruptions cast shadow over the African monsoon and the flow of the Nile, *Geophys. Res. Lett.*, *33*, L18711, doi:10.1029/2006GL027665.
Otterå, O. (2008), Simulating the effects of the 1991 Mount Pinatubo volcanic eruption using the ARPEGE atmosphere general circulation model, *Adv. Atmos. Sci.*, *25*, 213–226, doi:10.1007/s00376-008-0213-3.
Otto-Bliesner, B. L., E. C. Brady, J. Fasullo, A. Jahn, L. Landrum, S. Stevenson, N. Rosenbloom, A. Mai, and G. Strand (2016), Climate variability and change since 850 C.E.: An ensemble approach with the Community Earth System Model (CESM), *Bull. Am. Meteorol. Soc.*, *97*, 735–754, doi:10.1175/BAMS-D-14-00233.1.
Perlwitz, J., and H.-F. Graf (1995), The statistical connection between tropospheric and stratospheric circulation of the Northern Hemisphere in winter, *J. Clim.*, *8*, 2281–2295.
Predybaylo, E., G. L. Stenchikov, A. T. Wittenberg, and F. Zeng (2017), Impacts of a Pinatubo-size volcanic eruption on ENSO, *J. Geophys. Res. Atmos.*, *122*, 925–947, doi:10.1002/2016JD025796.
Robock, A. (2000), Volcanic eruptions and climate, *Rev. Geophys.*, *38*, 191–219, doi:10.1029/1998RG000054.

Robock, A., and Y. Liu (1994), The volcanic signal in Goddard Institute for Space Studies three-dimensional model simulations, *J. Clim.*, *7*, 44–55.
Robock, A., and J. Mao (1992), Winter warming from large volcanic eruptions, *Geophys. Res. Lett.*, *19*, 2405–2408, doi:10.1029/92GL02627.
Robock, A., and J. Mao (1995), The volcanic signal in surface temperature observations, *J. Clim.*, *8*, 1086–1103.
Robock, A., K. Taylor, G. Stenchikov, and Y. Liu (1995), GCM evaluation of a mechanism for El Niño triggering by the El Chichón ash cloud, *Geophys. Res. Lett.*, *22*, 2369–2372, doi:10.1029/95GL02065.
Rotstayn, L. D., and U. Lohmann (2002), Tropical rainfall trends and the indirect aerosol effect, *J. Clim.*, *15*, 2103–2116.
Sato, M., J. E. Hansen, M. P. McCormick, and J. B. Pollack (1993), Stratospheric aerosol optical depths, 1850–1990, *J. Geophys. Res.*, *98*(D12), 22,987–22,994, doi:10.1029/93JD02553.
Schmidt, G. A., et al. (2011), Climate forcing reconstructions for use in PMIP simulations of the last millennium (v1.0), *Geosci. Model Dev.*, *4*, 33–45, doi:10.5194/gmd-4-33-2011.
Self, S., M. R. Rampino, J. Zhao, and M. G. Katz (1997), Volcanic aerosol perturbations and strong El Niño events: No general correlation, *Geophys. Res. Lett.*, *24*, 1247–1250, doi:10.1029/97GL01127.
Shindell, D. T., G. A. Schmidt, M. E. Mann, and G. Faluvegi (2004), Dynamic winter climate response to large tropical volcanic eruptions since 1600, *J. Geophys. Res.*, *109*, D05104, doi:10.1029/2003JD004151.
Sigl, M., et al. (2014), Insights from Antarctica on volcanic forcing during the Common Era, *Nat. Clim. Change*, *4*, 693–697, doi:10.1038/NCLIMATE2293.
Sigl, M., et al. (2015), Timing and climate forcing of volcanic eruptions for the past 2,500 years, *Nature*, *523*, 543–549, doi:10.1038/nature14565.
Solomon, S. (1999), Stratospheric ozone depletion: A review of concepts and history, *Rev. Geophys.*, *37*, 275–316, doi:10.1029/1999RG900008.
Stenchikov, G. L., I. Kirchner, A. Robock, H.-F. Graf, J. C. Antuña, R. Grainger, A. Lambert, and L. Thomason (1998), Radiative forcing from the 1991 Mount Pinatubo volcanic eruption, *J. Geophys. Res.*, *103*, 13,837–13,857, doi:10.1029/98JD00693.
Stenchikov, G., A. Robock, V. Ramaswamy, M. D. Schwarzkopf, K. Hamilton, and S. Ramachandran (2002), Arctic Oscillation response to the 1991 Mount Pinatubo eruption: Effects of volcanic aerosols and ozone depletion, *J. Geophys. Res.*, *107*(D24), 4803, doi:10.1029/2002JD002090.
Stenchikov, G., K. Hamilton, A. Robock, V. Ramaswamy, and M. D. Schwarzkopf (2004), Arctic Oscillation response to the 1991 Pinatubo eruption in the SKYHI GCM with a realistic Quasi-Biennial Oscillation, *J. Geophys. Res.*, *109*, D03112, doi:10.1029/2003JD003699.
Stenchikov, G., K. Hamilton, R. J. Stouffer, A. Robock, V. Ramaswamy, B. Santer, and H.-F. Graf (2006), Arctic Oscillation response to volcanic eruptions in the IPCC AR4 climate models, *J. Geophys. Res.*, *111*, D07107, doi:10.1029/2005JD006286.
Stevenson, S., B. Otto-Bliesner, J. Fasullo, and E. Brady (2016), El Niño-like hydroclimate responses to last millennium volcanic eruptions, *J. Clim.*, *29*, 2907–2921, doi:10.1175/JCLI-D-15-0239.1.
Stevenson, S., J. T. Fasullo, B. L. Otto-Bliesner, R. A. Tomas, and C. Gao (2017), Role of eruption season in reconciling model and proxy responses to tropical volcanism, *Proc. Natl. Acad. Sci.*, *114*(8), 1822–1826, doi:10.1073/pnas.1612505114.
Taylor, K. E., R. J. Stouffer, and G. A. Meehl (2012), An overview of CMIP5 and the experiment design, *Bull. Am. Meteorol. Soc.*, *93*, 485–498, doi:10.1175/BAMS-D-11-00094.1.
Thomas, M. A., C. Timmreck, M. A. Giorgetta, H.-F. Graf, and G. Stenchikov (2009), Simulation of the climate impact of Mt. Pinatubo eruption using ECHAM5—Part 1: Sensitivity to the modes of atmospheric circulation and boundary conditions, *Atmos. Chem. Phys.*, *9*, 757–769.
Thompson, D. W. J., and J. M. Wallace (1998), The Arctic Oscillation signature in the wintertime geopotential height and temperature fields, *Geophys. Res. Lett.*, *25*, 1297–1300, doi:10.1029/98GL00950.
Tilmes, S., et al. (2013), The hydrological impact of geoengineering in the Geoengineering Model Intercomparison Project (GeoMIP), *J. Geophys. Res. Atmos.*, *118*, 11,036–11,058, doi:10.1002/jgrd.50868.
Timmreck, C. (2012), Modeling the climatic effects of large explosive volcanic eruptions, *Wiley Interdiscip. Rev. Clim. Change*, *3*, 545–564, doi:10.1002/wcc.192.
Toohey, M., K. Krüger, U. Niemeier, and C. Timmreck (2011), The influence of eruption season on the global aerosol evolution and radiative impact of tropical volcanic eruptions, *Atmos. Chem. Phys.*, *11*, 12 351–12 367, doi:10.5194/acp-11-12351-2011.
Toohey, M., K. Krüger, and C. Timmreck (2013), Volcanic sulfate deposition to Greenland and Antarctica: A modeling sensitivity study, *J. Geophys. Res. Atmos.*, *118*, 4788–4800, doi:10.1002/jgrd.50428.
Toohey, M., K. Krüger, M. Bittner, C. Timmreck, and H. Schmidt (2014), The impact of volcanic aerosol on the Northern Hemisphere stratospheric polar vortex: Mechanisms and sensitivity to forcing structure, *Atmos. Chem. Phys.*, *14*(11), 13 063–13 079, doi:10.5194/acp-14-13063-2014.
Toohey, M., K. Krüger, M. Sigl, F. Stordal, and H. Svensen (2016), Climatic and societal impacts of a volcanic double event at the dawn of the Middle Ages, *Clim. Change*, *136*, 401–412, doi:10.1007/s10584-016-1648-7.
Wahl, E. R., H. F. Diaz, J. E. Smerdon, and C. M. Ammann (2014), Late winter temperature response to large tropical volcanic eruptions in temperate western North America: Relationship to ENSO phases, *Global Planet. Change*, *122*, 238–250.
Zambri, B., and A. Robock (2016), Winter warming and summer monsoon reduction after volcanic eruptions in Coupled Model Intercomparison Project 5 (CMIP5) simulations, *Geophys. Res. Lett.*, *43*, 10,920–10,928, doi:10.1002/2016GL070460.
Zanchettin, D., et al. (2016), The Model Intercomparison Project on the climatic response to volcanic forcing (VolMIP): Experimental design and forcing input data for CMIP6, *Geosci. Model Dev.*, *9*, 2701–2719, doi:10.5194/gmd-9-2701-2016.